EES Catalysis

PAPER

View Article Online
View Journal | View Issue

Cite this: *EES Catal.*, 2023, 1, 987

OER highly active encapsulants to improve the electrochemical anticorrosion of Fe–N–C for ultralong-lifespan and high-rate rechargeable zinc–air batteries†

Jiale Li,[a] Niu Huang,*[a] Minghui Lv,[a] Na Su,[c] Chao Li,[a] Yingping Huang,[a] Yongye Wang,[a] Yong Zheng,[a] Wei Liu,[a] Tianyi Ma*[b] and Liqun Ye*[a]

Received 7th July 2023,
Accepted 27th July 2023

DOI: 10.1039/d3ey00160a

rsc.li/eescatalysis

Fe–N–C has been exploited as a promising oxygen reduction reaction (ORR) electrocatalyst. However, carbon corrosion and corresponding coordination structure destruction inevitably happen upon exposure at high potentials. Even under low potentials, the byproduct peroxide generated in 2-electron ORR processes produces radicals such as •OH and •OOH with Fe-center allies *via* Fenton-like reactions to destroy catalyst structures. In this work, we designed a composite, wherein each N-doped carbon nanotube with Fe nanoparticles encapsulated in the Fe-NCNT is uniformly and tightly wrapped by vertically grown NiFe-layered double hydroxide (LDH) nanosheets. During the charging process of Zn–air batteries (ZABs), the external NiFe-LDH preferentially catalyzes oxygen evolution reactions (OERs), and thus the internal Fe-NCNT could simply act as a carbon skeleton to transfer electrons. Moreover, the Fe-NCNT@NiFe-LDH displays a strikingly high peroxide disproportionation rate and superior electrocatalytic activities towards peroxide reduction and oxidation reactions. Thus, the radical corrosion is enormously reduced. The Fe-NCNT@NiFe-LDH delivers a record-refresh overpotential difference of 0.52 V, surpassing that of recently reported state-of-the-art bifunctional oxygen electrocatalysts. The composite-based ZABs demonstrate long discharging/charging lifespans and excellent rate performances, *e.g.* over 5000 cycles (near 1743 h) at 50 mA cm^{-2}.

Broader context

Transition metal and nitrogen co-doped carbon (TM–N–C) catalysts have been extensively investigated, and they demonstrated desirable ORR catalytic activities. In particular, ORR highly active Fe–N–C is a current research priority. However, this advanced non-noble metal catalyst encounters serious challenges such as low durability, presumably stemming from electrochemical oxidation especially at high working potentials (OER-occurring potential scope) and radical (such as •OH)-caused damage. In this work, to lessen and even avoid the irreversible carbon corrosion and corresponding coordination structure destruction, we prepared a Fe–N–C catalyst composed of high-density, well-dispersed, and highly exposed N-doped carbon nanotubes with Fe nanoparticles embedded within. Then, thin NiFe-LDH nanosheets were vertically grown on the surface of each nanotube to make an intimate and well-enwrapped core–shell structure. During the charging process of Zn–air batteries (ZABs), the external NiFe-LDH preferentially catalyzes OERs. The Fe-NCNT@NiFe-LDH displays a strikingly fast peroxide disproportionation rate and superior electrocatalytic activities towards peroxide reduction and oxidation reactions. Thus, the radical corrosion is enormously depressed. The composite-based ZABs demonstrate long discharging/charging lifespans and excellent rate performances.

Introduction

The increasing depletion of fossil energy and emergence of various environmental problems have attracted increasing attention towards clean energies and corresponding advanced technologies.[1,2] During the past three decades, an assortment of rechargeable batteries have emerged and developed. Among them, zinc–air batteries (ZABs), with the advantages of high energy density (1084 W h kg^{-1}), low cost, and environmental friendliness (aqueous batteries), have been considered one of the

[a] College of Materials and Chemical Engineering, Key Laboratory of Inorganic Nonmetallic Crystalline and Energy Conversion Materials, China Three Gorges University, Yichang 443002, China. E-mail: huangliu.ysxf@163.com, lqye@ctgu.edu.cn
[b] School of Science, RMIT University, Melbourne, VIC 3000, Australia. E-mail: tianyi.ma@rmit.edu.au
[c] School of New Energy and Materials, Southwest Petroleum University, Chengdu 610500, China

† Electronic supplementary information (ESI) available. See DOI: https://doi.org/10.1039/d3ey00160a

most promising energy conversion and storage technologies.[3–5] Unfortunately, there are several limitations such as the sluggish kinetics of oxygen evolution reactions (OERs) and oxygen reduction reactions (ORRs) occurring at the air cathodes in cell charging and discharging processes hampering the application of rechargeable ZABs.[6–8] Although benchmark Pt/C and Ir or Ru oxides respectively possess efficient ORR and OER electrocatalytic activities, their poor stability, low storage capacity, and high cost are application barriers. Clearly, nonprecious-metal-containing electrocatalysts with excellent OER and ORR activities and stability are highly worth pursuing for developing conventional two-electrode rechargeable ZABs.[9]

Transition metal and nitrogen co-doped carbon (TM–N–C, M = Fe, Mn, Co, Ni, *etc.*) catalysts have been extensively investigated, and they demonstrated desirable ORR catalytic activities, originating from TM–N_x active species, N–C configurations such as pyridinic-N and graphitic N, and TM-catalyzing increased the carbon graphitization degree and N doping level.[10–12] In particular, ORR highly active Fe–N–C is a current research priority.[13–15] However, this advanced non-noble metal catalyst encounters serious challenges such as low durability, presumably stemming from electrochemical oxidation especially at high working potentials (OER-occurring potential scope),[16] and radical (such as $^{\bullet}OH$)-caused damage.[17] In the discharging process of ZABs, peroxides are generated as byproducts, and their Fenton-like reactions with Fe-center allies will produce $^{\bullet}OH$ radicals that are highly reactive.[17] $^{\bullet}OH$ radicals can damage catalyst structures *via* two pathways. One involves the conversion of the carbon substrate to CO_2, resulting in carbon corrosion and the stripping or leaching of metal active centers.[16] Another involves the grafting of oxygen functional groups on the catalyst surface, critically accounting for the electrocatalytic performance attenuation.[18,19]

To address the issue of the inferior OER activities of Fe–N–C-based catalysts, it was proposed to grow NiFe-based layered double hydroxides (NiFe-LDHs featuring exceptional OER catalytic activities) on the surface of Fe–N–C-based catalysts.[20,21] Furthermore, the ion and electron pathways could be reciprocally strengthened by hydrophilic NiFe-LDHs and conductive TM–N–C, synergistically contributing to the bifunctionality improvement of the TM–N–C/NiFe-LDH composite towards ORRs and OERs, exceeding that of its corresponding pure components.[22,23] Additionally, when Fe–N–C as the core is wrapped/coated by other materials, the out-layer will protect the under-layer physically at least, thus alleviating Fe–N–C corrosion.[24,25] When ZABs are in the charging process, OH^- could be oxidized (forming O_2) preferentially at the NiFe-LDH out-layer to let the under-layer Fe–N–C to rest (the catalyzing role of Fe–N–C on OERs is exempted). More importantly, the introduction of a NiFe-LDH wrapper to Fe–N–C probably regulates the peroxide decomposition paths away from Fenton-like reactions to avoid radical generation and attack. It can be speculated that the Fe–N–C durability is remarkably enhanced by well and tightly enwrapping OER highly active NiFe-LDHs.

Herein, to lessen and even avoid the irreversible carbon corrosion and corresponding coordination structure destruction, we prepared a Fe–N–C catalyst composed of high-density, well-dispersed, and highly exposed N-doped carbon nanotubes with Fe nanoparticles embedded in. Then, thin NiFe-LDH nanosheets were vertically grown on the surface of each nanotube to make an intimate and well-enwrapped core–shell structure. The prepared Fe-NCNT@NiFe-LDH exhibited exceptional electrocatalytic activities with an overpotential of 180 mV at 10 mA cm^{-2} for OERs, exceeding the OER performance of NiFe-LDHs; and with a half-wave potential ($E_{1/2}$) of 0.89 V for ORRs, superior to the ORR performance of Fe-NCNTs. It was found that the disproportionation of the Fe-NCNT@NiFe-LDH on H_2O_2 was highly efficient, more prominent than the pure Fe-NCNT with regard to the oxygen production rate and amount. Simultaneously, the composite exhibited electrocatalytic abilities towards peroxide reduction and oxidation reactions. The risk of free radical production (*via* consuming H_2O_2 through Fenton-like reactions) was substantially decreased. More importantly, due to the wrapping protective effect of the NiFe-LDH, the Fe-NCNT@NiFe-LDH represented much better anticorrosion performance at high potentials, which could keep the ORR electrocatalytic activity even after the OER (as revealed by the OER–ORR cycling hold test), while the Fe-NCNT lost most ORR performance after the OER. As expected, the composite assembled ZABs achieved high efficiency and robust rechargeability, as revealed by the extremely long charging/discharging cycle time and low voltage gap, *e.g.* 1777 h with a voltage gap of 0.73 V at 10 mA cm^{-2}, 1743 h with a voltage gap of 0.96 V at 50 mA cm^{-2}, and 80 h with a voltage gap of 1.39 V at 100 mA cm^{-2}.

Results and discussion

Fig. 1(a) schematically depicts the preparation processes of the Fe-NCNT@NiFe-LDH. First, a piece of carbon cloth (CC) was immersed into an aqueous solution of ferrous citrate and urea and kept at 95 °C for 3 h *via* chemical bath deposition (CBD) to grow $FeO_x(OH)_y$ *in situ*, which functions as the precursor to provide Fe for the catalytic growth of carbon nanotubes (SEM images are shown in Fig. S1 in ESI†), and it was then coated with polydopamine (PDA). Second, the Fe-NCNT was synthesized by chemical vapor deposition (CVD) using $FeO_x(OH)_y$@PDA (SEM image is shown in Fig. S2, ESI†) as the precursor pyrolyzed at 900 °C for 2 h with dicyandiamide as the solid N/C source. Third, vertically aligned NiFe-LDH nanosheets were compactly and uniformly grown on each Fe-NCNT surface *via* similar CBD. Fig. 1(b) and (c) shows the low- and high-magnification scanning electron microscopic (SEM) images of the Fe-NCNT, respectively. As revealed in the images, the Fe-NCNTs with a diameter of 100–400 nm are of high density and well dispersion, which promotes the achievement of abundant active sites (Fe–N_x and N–C configurations for ORRs[10–12]) with high exposure and simultaneously facilitates the subsequent NiFe-LDH coating (which functions as OER active site sources). Fig. 1(d) displays the transmission electron microscopic (TEM) image of the Fe-NCNT, intuitively suggesting that the Fe-NCNT is of nanotube structure with nanoparticles embedded. The high-resolution (HR) TEM image (Fig. 1(e)) demonstrates that

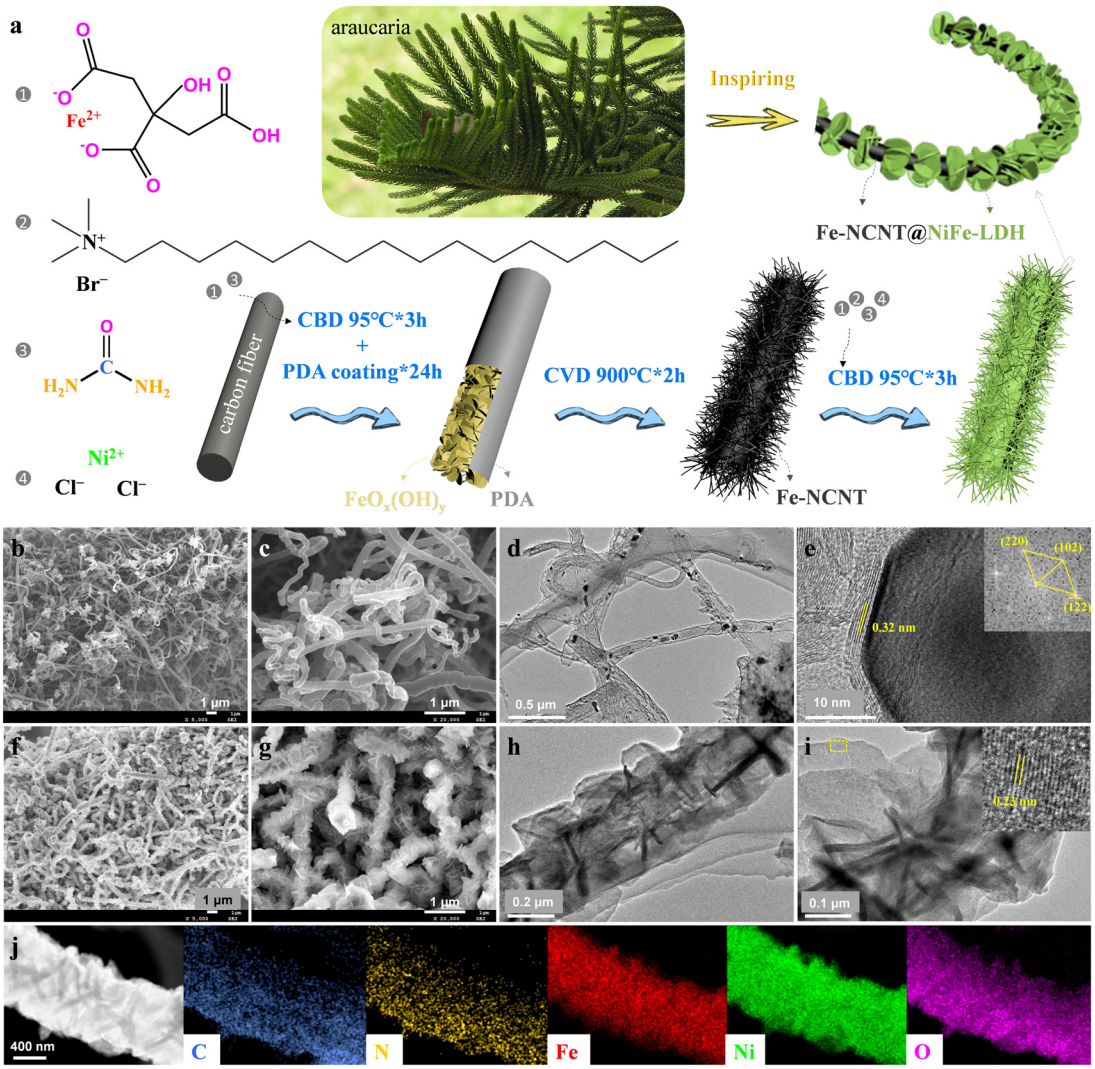

Fig. 1 (a) Preparation process and microstructure demonstration of the Fe-NCNT@NiFe-LDH. (b) Low-magnification and (c) high-magnification SEM images of the Fe-NCNT. (d) and (e) HRTEM images of the Fe-NCNT with FT plots of the Fe_3C nanoparticle inserted. (f) Low-magnification and (g) high-magnification SEM images of the Fe-NCNT@NiFe-LDH. (h) and (i) HRTEM images of the Fe-NCNT@NiFe-LDH with partial enlargement of the NiFe-LDH inserted. (j) EDS mapping of the Fe-NCNT@NiFe-LDH.

the encapsulated particle is of Fe_3C phase, as revealed by the inserted Fourier transform (FT). The Fe_3C nanoparticle is enwrapped by a graphitized carbon layer with a lattice spacing of 0.32 nm, corresponding to the (002) plane of graphitic carbon. The X-ray diffraction (XRD) pattern of the Fe-NCNT is shown in Fig. 2(a), where a diffraction peak located at $\sim 26^\circ$ is indexed to the 2H graphitic carbon (002) plane (PDF# 41-1487), and other diffraction peaks correspond well to Fe_3C (PDF# 35-0772). The low- (Fig. 1(f)) and high-magnification (Fig. 1(g)) SEM images of the Fe-NCNT@NiFe-LDH clearly demonstrate that the Fe-NCNTs are uniformly and tightly covered by NiFe-LDH nanosheets. In addition, the nanosheets with a thickness of 10–20 nm are vertically aligned on the Fe-NCNT surface, as clearly illustrated by the TEM images (Fig. 1(h) and (i)). Notably, hexadecyl trimethyl ammonium bromide (CTAB) was introduced in the CBD process to grow NiFe-LDH nanosheets. Without the surfactant, the NiFe-LDH nanosheets grown are relatively nonuniform, as revealed in Fig. S3 (ESI†). The inserted HRTEM image in Fig. 1(i) displays a lattice spacing of 0.23 nm, corresponding well to the NiFe-LDH (015) plane. (More HRTEM images of the NiFe-LDH component are provided in Fig. S4 in ESI.†) Similarly, as shown in Fig. 2(a), the other diffraction peaks of the Fe-NCNT@NiFe-LDH catalyst (in comparison with Fe-NCNT) correspond well to the NiFe-LDH phase (PDF# 40-0215). Additionally, Fig. 1(j) shows the energy-dispersive X-ray spectroscopy (EDS) elemental mappings of the Fe-NCNT@NiFe-LDH. Its composition elements including C, N, Fe, Ni, and O are uniformly distributed in the whole sample range. Notably, the uniform and dense green spots (representing Ni element) suggest that NiFe-LDH nanosheets are uniformly distributed on the Fe-NCNT core and the core is completely coated by the NiFe-LDH shell.

The compositions and element states of the Fe-NCNT@NiFe-LDH, Fe-NCNT and NiFe-LDH were characterized by X-ray photoelectron spectroscopy (XPS). Fig. 2(b) shows the XPS

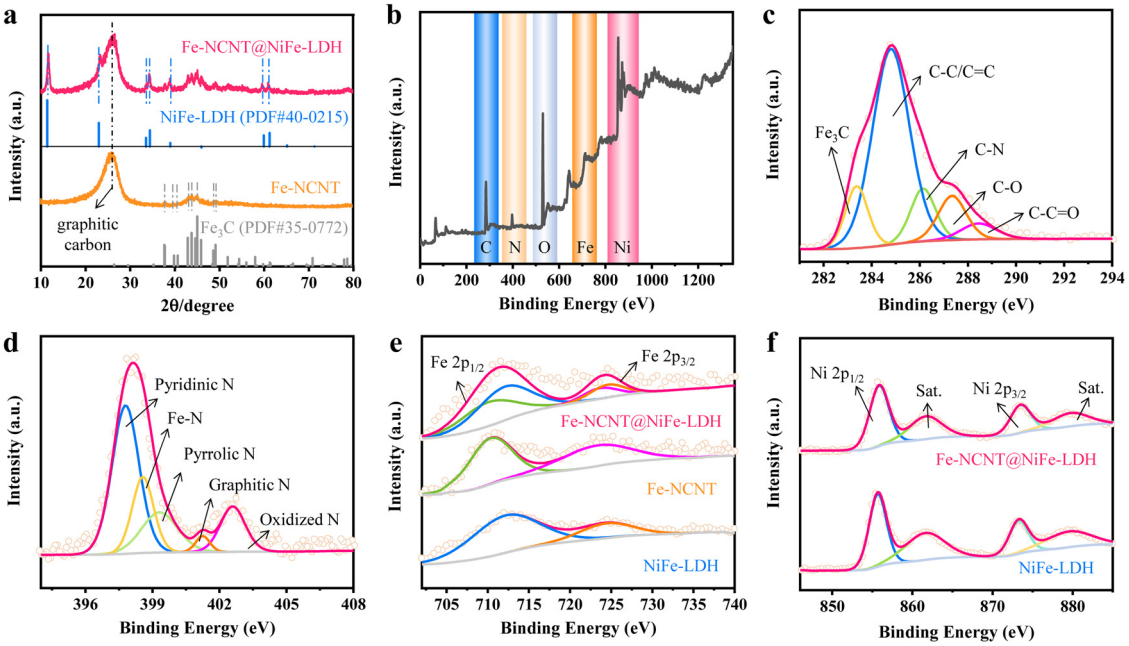

Fig. 2 (a) XRD patterns of the Fe-NCNT@NiFe-LDH and Fe-NCNT. (b) XPS survey spectra, (c) C 1s spectra, and (d) N 1s spectra of the Fe-NCNT@NiFe-LDH. High-resolution XPS spectra of (e) Fe 1s and (f) Ni 2p for the Fe-NCNT@NiFe-LDH and its counterparts.

survey spectrum of the Fe-NCNT@NiFe-LDH, revealing that it contains Fe, Ni, C, N, and O elements. Fig. 2(c) exhibits its high-resolution C 1s spectrum, where the peaks at 283.4, 284.8, 286.2, 287.4, and 288.5 eV are assigned to Fe_3C, C–C/C═C,

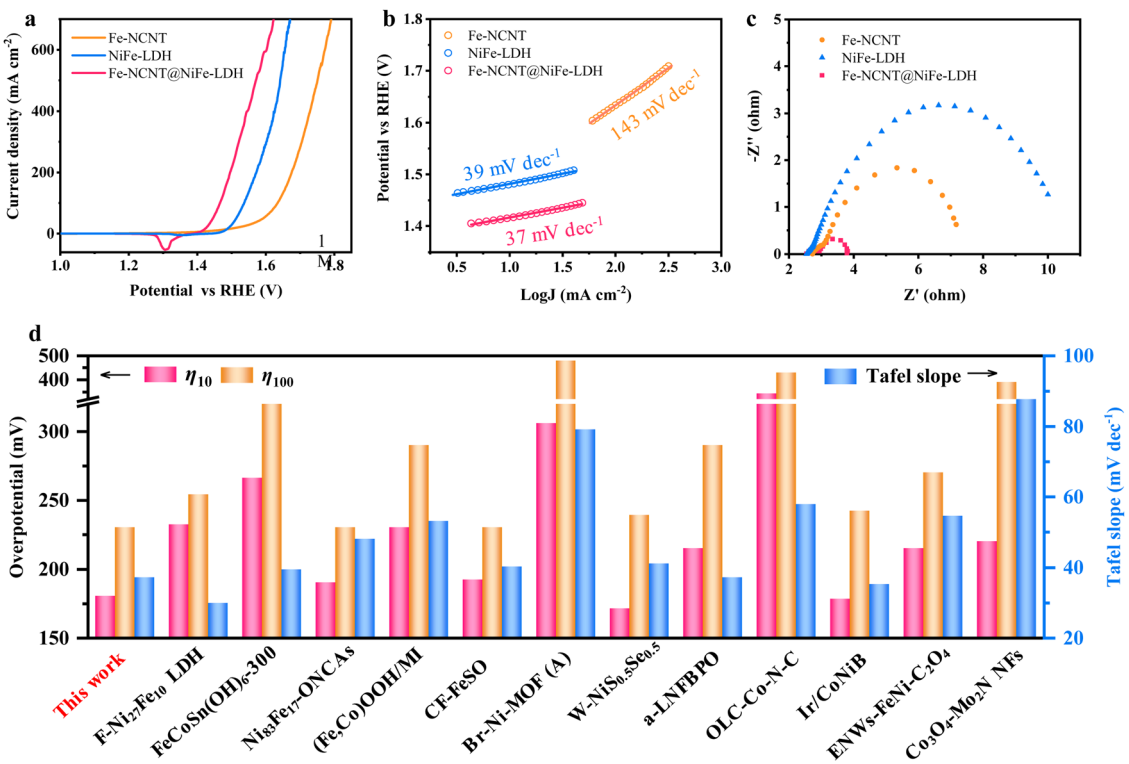

Fig. 3 (a) OER–LSV curves, (b) corresponding Tafel slope plots, and (c) EIS spectra of the Fe-NCNT, NiFe-LDH, and Fe-NCNT@NiFe-LDH, measured in O_2-saturated 1 M KOH. Notes: except for special instructions, catalysts grown *in situ* or grown on CC substrates are directly used for tests without rotation (powdery samples usually only for RRDE and RDE). (d) Summary of the OER performance of several recently reported superior OER electrocatalysts, in terms of the overpotentials (η_{10} and η_{100}) corresponding to 10 and 100 mA cm^{-2} respectively as well as the Tafel slope.

C–N, C–O, and C–C═O. Fig. 2(d) shows its high-resolution N 1s spectrum, where the peaks at 397.8, 398.6, 399.3, 401.3, and 402.7 eV are assigned to pyridinic, Fe–N, pyrrolic, graphitic, and oxidized N. Among them, the Fe–N and pyridinic N are considered to be the most active sources for ORRs. Fig. 2(e) shows the high-resolution Fe 2p spectra of the Fe-NCNT@NiFe-LDH, pure Fe-NCNT and NiFe-LDH. The Fe $2p_{3/2}$ peaks of the Fe-NCNT@NiFe-LDH can be separated into two peaks, separately corresponding to the Fe species from the NiFe-LDH and Fe-NCNT. The result is consistent with the XRD patterns. As for the high-resolution Ni 2p spectra (Fig. 2(e)), the Fe-NCNT@NiFe-LDH shows almost the same spectrum as that of the NiFe-LDH, with two peaks at 855.8 (Ni $2p_{3/2}$) and 873.5 eV (Ni $2p_{1/2}$) and two satellite peaks (Sat.) at 861.9 and 879.9 eV. These results firmly confirm the successful preparation of the Fe-NCNT@NiFe-LDH.

To evaluate the OER electrocatalytic performance, related tests were performed using a three-electrode system in 1 M KOH electrolyte. The OER linear sweep voltammetry (LSV) curves display that the Fe-NCNT@NiFe-LDH possesses the lowest overpotential of 180 mV to reach a current density of 10 mA cm^{-2} and demands only an overpotential of 230 mV for 100 mA cm^{-2} current density (Fig. 3(a)), which is much smaller than those of the NiFe-LDH and Fe-NCNT. Fig. S5 (ESI†) shows the CV curves (without *iR* compensation) of the Fe-NCNT@NiFe-LDH, Fe-NCNT, and NiFe-LDH. The CV result is in agreement with the LSV result, suggesting the same OER trend: the Fe-NCNT@NiFe-LDH superior to the NiFe-LDH, and the NiFe-LDH surpassing the Fe-NCNT. As displayed in Fig. 3(b), the Fe-NCNT@NiFe-LDH demonstrates a Tafel slope of 37 mV dec^{-1}, smaller than those of the Fe-NCNT (143 mV dec^{-1}) and NiFe-LDH (39 mV dec^{-1}). The extremely low Tafel slope suggests that the Fe-NCNT@NiFe-LDH possesses excellent OER kinetics. Similarly, as shown in the electrochemical impedance spectroscopy (EIS) Nyquist plots (Fig. 3(c)), the composite exhibits a charging-transfer resistance (R_{ct}) of 0.90 Ω, much lower than that of the corresponding pure components. The lowest R_{ct} value manifests the fastest charge-transfer rate at the catalyst/electrolyte interface, in accordance with the Tafel result. Specifically, despite the high intrinsic OER activity of the NiFe-LDH, its inherent insulation property leads to a larger R_{ct} of 7.44 Ω, while because of the

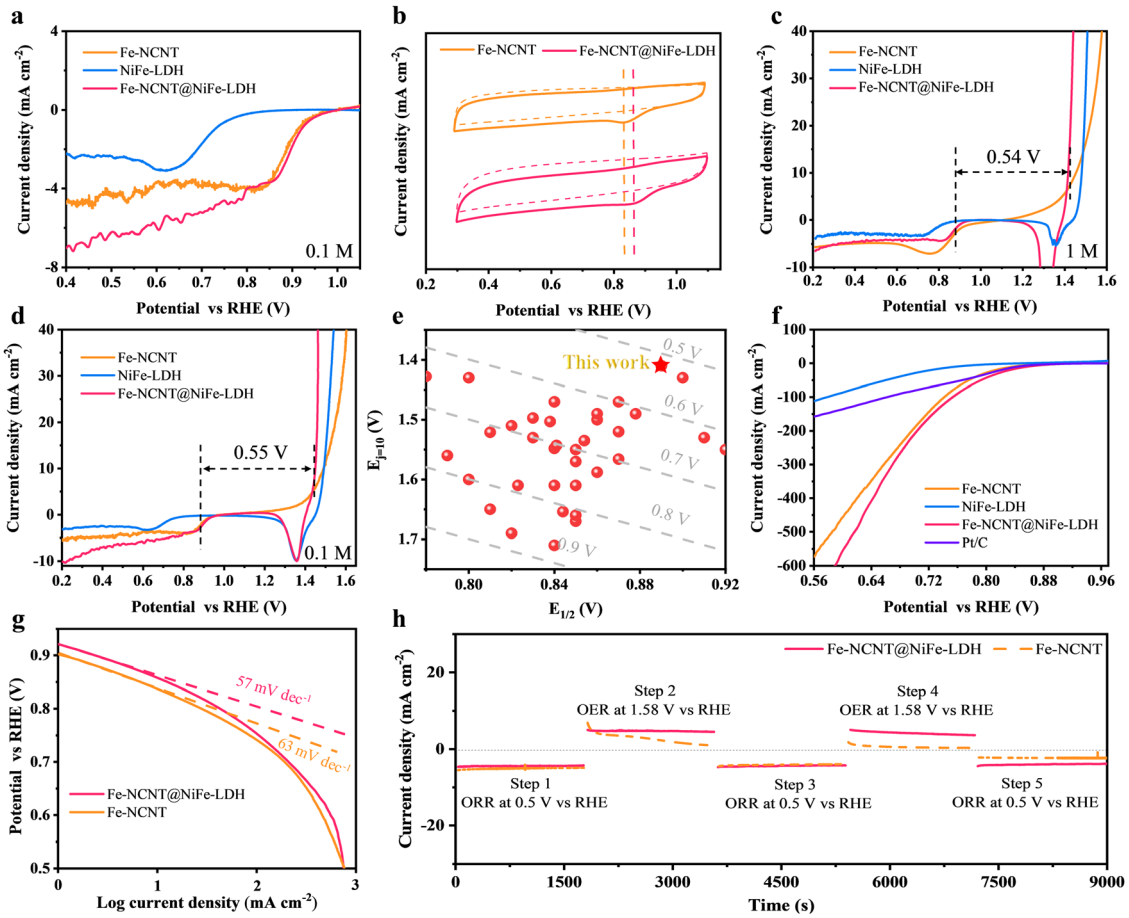

Fig. 4 (a) ORR–LSV curves of the Fe-NCNT@NiFe-LDH, Fe-NCNT and NiFe-LDH, measured in O_2-saturated 0.1 M KOH. (b) CV curves of the Fe-NCNT@NiFe-LDH and Fe-NCNT, measured in N_2-saturated (thin dotted lines) and O_2-saturated (thick lines) 0.1 M KOH solutions. LSV curves of the Fe-NCNT@NiFe-LDH, Fe-NCNT, and NiFe-LDH measured in O_2-saturated (c) 1 M KOH and (d) 0.1 M KOH alkaline electrolytes. (e) Summary of recently reported Δ*E* of excellent electrocatalysts, compared with the as-prepared Fe-NCNT@NiFe-LDH. (f) ORR polarization curves of the Fe-NCNT@NiFe-LDH, Fe-NCNT, NiFe-LDH, and Pt/C measured by the GDE. (g) Corresponding Tafel slope plots of the Fe-NCNT@NiFe-LDH and Fe-NCNT. (h) Chronoamperometric ORR/OER-cycle curves of the Fe-NCNT@NiFe-LDH and Fe-NCNT.

intrinsic conductor property, the Fe-NCNT has a smaller R_{ct} value of 4.45 Ω. The OER electrocatalytic activity of the Fe-NCNT@NiFe-LDH prepared in this work is preeminent, in terms of overpotentials at 10 and 100 mA cm^{-2} and Tafel slope, even compared with the recently reported state-of-the-art OER electrocatalysts (Fig. 3(d)).[9,26–36] Their detailed performance parameters are concluded in Table S1 in ESI.† The long-term chronopotentiometric response of the Fe-NCNT@NiFe-LDH is displayed in Fig. S6a (ESI†). As revealed, the working potential of the Fe-NCNT@NiFe-LDH could be kept at 1.46–1.47 V *vs.* RHE without fluctuation or augment. Moreover, after a long-term chronopotentiometric test, the OER–LSV curve is almost completely overlapped with its initial curve (Fig. S6b, ESI†), disclosing its satisfactory durability for OERs. As for the Fe-NCNT and NiFe-LDH, they exhibit inferior stability (Fig. S7 and S8, ESI†). In particular, the Fe-NCNT demonstrates obvious performance reduction (Fig. S8, ESI†).

The ORR activities of these electrocatalysts were assessed by LSV measured in an O_2-saturated 0.1 M KOH solution, as shown in Fig. 4(a). The Fe-NCNT@NiFe-LDH demonstrates excellent electrocatalytic activity towards ORRs with an onset potential (E_{onset}) of 0.98 V and a half-wave potential ($E_{1/2}$) of 0.89 V, in contrast to the Fe-NCNT (E_{onset} of 0.98 V and $E_{1/2}$ of 0.88 V) and NiFe-LDH (E_{onset} of 0.81 V and $E_{1/2}$ of 0.69 V). Fig. 4(b) displays the cyclic voltammogram (CV) curves of Fe-NCNT@NiFe-LDH and Fe-NCNT in O_2- and N_2-saturated 0.1 M KOH solutions, respectively. Compared with CV curves collected under N_2 saturation conditions, distinct reduction protuberances emerge in the CV curves collected under O_2-saturated conditions, indicating that ORRs occurred on the Fe-NCNT@NiFe-LDH and Fe-NCNT. In addition, the oxygen reduction peak of the Fe-NCNT@NiFe-LDH emerges earlier (corresponding to higher potential) than that of the Fe-NCNT, suggesting that the former catalyst possesses superior ORR activity, which is in agreement with the LSV result shown in Fig. 4(a). The OER and ORR bifunctional performances of these electrocatalysts were evaluated using an overpotential difference, *i.e.* ΔE, which is equal to the difference between the OER potential at 10 mA cm^{-2} and the ORR half-wave potential ($\Delta E = E_{j=10} - E_{1/2}$). Fig. 4(c) displays the OER–ORR LSV curves of the Fe-NCNT@NiFe-LDH, Fe-NCNT, and NiFe-LDH in O_2-saturated 1 M KOH, respectively, where the Fe-NCNT@NiFe-LDH exhibits a ΔE of only 0.54 V, much superior to the Fe-NCNT (0.61 V) and NiFe-LDH (0.70 V). Similarly, when measured in O_2-saturated 0.1 M KOH (Fig. 4(d)), the Fe-NCNT@NiFe-LDH also has an excellent ΔE value of 0.55 V, much smaller than those of the Fe-NCNT (0.60 V) and NiFe-LDH (0.80 V). Detailed OER–ORR performance parameters in 0.1 and 1 M KOH are concluded in Tables S2 and S3 (ESI†). For comparison with other electrocatalysts, ΔE is calculated according to the difference between the $E_{j=10}$ of OERs in 1 M KOH and $E_{1/2}$ of ORRs in 0.1 M KOH. The ΔE values from the recent studies reported in the literature are summarized in Fig. 4(e) (and Table S4, ESI†). As revealed, the Fe-NCNT@NiFe-LDH demonstrates the lowest ΔE value of 0.52 V.[9,22,37–72] Lower ΔE suggests higher OER and ORR electrocatalytic activities to promise better reversibility of the O_2/OH^- redox couple. Importantly, high reversibility is in desperate need for rechargeable ZABs to improve the energy efficiency and long-term cycling performance. Notably, the OER and ORR LSV curves of the Fe-NCNT prepared at different CVD temperatures are shown in Fig. S9 (ESI†). In addition, by comparing the ΔE values, the CVD temperature was determined to be 900 °C the for Fe-NCNT@NiFe-LDH. Clearly, the Fe-NCNT@NiFe-LDH possesses excellent OER and ORR activities, stemming from the excellent OER activity of the NiFe-LDH, the eminent ORR activity of the Fe-NCNT, and the synergy between the two components. Notably, the OER and ORR reproducibilities of the Fe-NCNT@NiFe-LDH and Fe-NCNT are shown in Fig. S10 (ESI†). The enhancement in ORR results from the improved hydrophilicity of the Fe-NCNT after wrapping with the NiFe-LDH. As demonstrated in Fig. S11 and Movie S1 (ESI†), the Fe-NCNT exhibits strong hydrophobicity with a contact angle of 139°. Due to the intrinsic hydrophilic property of the NiFe-LDH, the Fe-NCNT@NiFe-LDH becomes strongly hydrophilic. As revealed in Movie S2 (ESI†), water droplets quickly moisten the surface of the Fe-NCNT@NiFe-LDH with a contact angle of ~0°. Because of improvement in hydrophilicity, the electrochemically active surface area (ECSA) of the Fe-NCNT@NiFe-LDH is significantly increased compared with the Fe-NCNT (Fig. S12–S14, ESI†). Consequently, the ion pathway is strengthened to result in favorable ORR performance.[37] Simultaneously, the cooperative effect on the OER originates from the strengthened electron pathway. The OER performance of the NiFe-LDH is restricted by its inherent insulation property. However, when grown *in situ* on the superior carbon nanotube network, the highly conductive electron pathway is established for the NiFe-LDH to electrocatalyze OERs. As verified by the EIS measurement (Fig. 3(c)), compared with the NiFe-LDH, the charging transfer resistance of the Fe-NCNT@NiFe-LDH is greatly reduced.

To further compare the ORR activities of these electrocatalysts and Pt/C, they were tested by a gas diffusion electrode method (GDE with its structure is shown in Fig. S15, ESI†).[73] As revealed in Fig. 4(f), the Fe-NCNT@NiFe-LDH achieves a current density of 550 mA cm^{-2}, larger than those of the Fe-NCNT (455 mA cm^{-2}), NiFe-LDH (90 mA cm^{-2}), and Pt/C (140 mA cm^{-2}) at 0.6 V *vs.* RHE. The Fe-NCNT@NiFe-LDH represents an ORR Tafel slope of 57 mV dec^{-1}, superior to that of the Fe-NCNT (63 mV dec^{-1}), as shown in Fig. 4(g). To evaluate the ORR stability, long-term chronoamperometric responses of the Fe-NCNT@NiFe-LDH and Fe-NCNT were monitored. As displayed in Fig. S16 and S17 (ESI†), the Fe-NCNT@NiFe-LDH and Fe-NCNT both could keep 100% current retention after continuous working at 0.5 V *vs.* RHE for 24 h. However, to simulate the alternate discharging/charging processes in rechargeable ZABs (ORR for discharging process and OER for charging process), chronoamperometric ORR/OER-cycle curves are suggested to be applied to evaluate the stability of ORR/OER-bifunctional electrocatalysts. As disclosed in Fig. 4(h), Fe-NCNT exhibits obvious attenuation in both OER and ORR stages. Notably, the Fe-NCNT has favorable ORR stability when only working in the ORR potential range (as shown in Fig. S16, ESI†), while after the OER, its ORR electrocatalytic activity obviously decayed (as shown in Fig. 4(g)). This suggests that working at high potentials (*i.e.* OER potential range)

damage the material structure of the Fe-NCNT. In contrast, the Fe-NCNT@NiFe-LDH basically maintains stable current densities in these ORR-OER cycles. Their discrepancy on stability can be attributed to the surface wrapping effects of the NiFe-LDH. When these NCNTs are wrapped tightly and uniformly with NiFe-LDH nanosheets, the external NiFe-LDH will preferentially catalyze the OER (during the ZAB charging process) because of its excellent OER electrocatalytic activity. Consequently, the internal Fe-NCNT need not participate in reactions, and it simply acts as a carbon skeleton to transfer electrons, thereby avoiding electrochemical oxidation and preventing, to some extent, structural damage and performance failure from happening. In fact, in electrochemical devices, the electrochemical oxidation could be more serious. For example, without NiFe-LDH encapsulation, Fe-NCNTs with a relatively poor OER electrocatalytic activity are required to work under a higher potential (with a larger overpotential) to reach the same OER current density during the charging process of ZABs. While under a higher potential, carbonaceous catalysts are more susceptible to electrochemical oxidation, structure damage and performance failure.[16]

Oxygen reduction can be classified into two pathways, namely, 4-electron transfer process (OH^- as the product) and 2-electron transfer process (H_2O_2 as the byproduct). RRDE as a common and useful technique is utilized to distinguish the 4-electron pathway from the 2-electron pathway, simultaneously estimating the total H_2O_2 generation ratio (%). As revealed in Fig. 5(a) and (b), the powdery Fe-NCNT@NiFe-LDH catalyst also demonstrates a more efficient ORR activity with a higher half-wave of 0.89 V in contrast to the Fe-NCNT of 0.87 V and Pt/C of 0.88 V *vs.* RHE. The H_2O_2 yields of the Fe-NCNT@NiFe-LDH and Fe-NCNT were calculated to be 0–6% with the electron transfer number (n) of 3.88–4.0 at a potential around 0.8 to 0.3 V *vs.* RHE. The NiFe-LDH powder exhibits worse ORR performance, coherent with the result illustrated in Fig. 4(a). Actually, the 4-electron ORR could be processed *via* a direct 4-electron pathway and/or a "2 + 2"-electron pathway, *i.e.* a 2-electron transfer process from O_2 to H_2O_2 plus a 2-electron transfer process from H_2O_2 to OH^- (where H_2O_2 acts as an ORR intermediator). However, the "2 + 2"-electron pathway cannot be distinguished from the direct 4-electron pathway *via* conventional RRDE. Here, we introduced a peroxidase-coupled RRDE method. (More details are provided

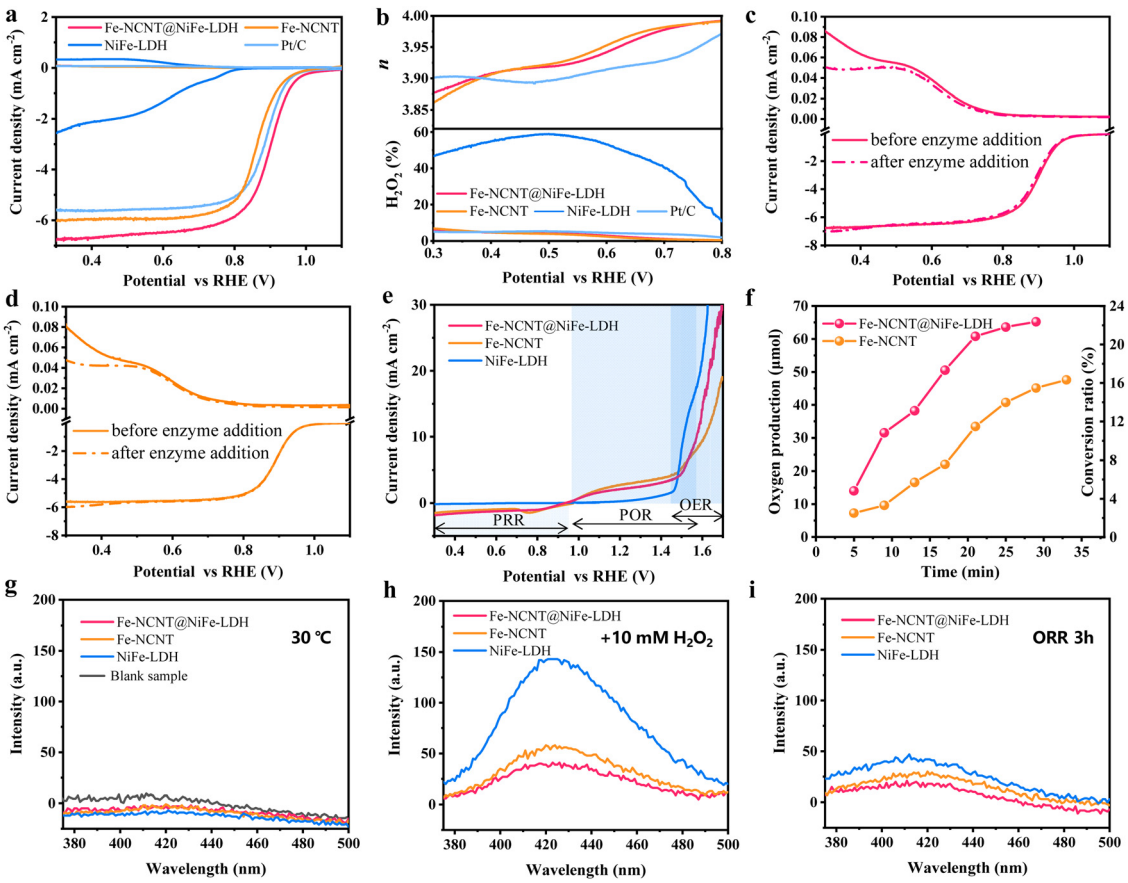

Fig. 5 (a) RRDE curves of the Fe-NCNT@NiFe-LDH, Fe-NCNT, NiFe-LDH, and Pt/C powders in O_2-saturated 0.1 M KOH at 1600 rpm. (b) H_2O_2 yield and electron transfer number (n) of these powdery catalysts. RRDE curves of (c) Fe-NCNT@NiFe-LDH and (d) Fe-NCNT powdery catalysts before and after the addition of peroxidase. (e) RDE curves of Fe-NCNT@NiFe-LDH, Fe-NCNT and NiFe-LDH powdery catalysts measured in N_2-saturated 0.1 M KOH with 10 mM H_2O_2 added and 1600 rpm rotation. (f) Oxygen production amount and disproportionation rate of H_2O_2 catalyzed by the Fe-NCNT@NiFe-LDH and Fe-NCN, respectively. Fluorescence spectra obtained from the PTA solution under the conditions of (g) 30 °C for 24 h, (h) 10 mM H_2O_2 added for 24 h, and (i) ORRs at 0.5 V *vs.* RHE for 3 h.

in ESI.†) In the presence of horseradish peroxidase, H_2O_2 can be embraced by the α-helixes and β-sheets and reduced by the center heme group of the peroxidase immediately.[74] As a result, the sequenced reduction of intermediate H_2O_2 on the disk electrode (in "2 + 2"-electron pathway) and the collection of by product-H_2O_2 by the ring electrode could be both disturbed or interfered. Fig. 5(c) and (d) demonstrate the RRDE curves of the Fe-NCNT@NiFe-LDH and Fe-NCNT before and after horseradish peroxidase addition. As expected, the currents in ring electrode are obviously dropped, suggesting that an amount of H_2O_2 is competitively captured by the peroxidase. Interestingly, there are almost no fluctuations in disk currents after adding the peroxidase, revealing that the nominal 4-electron pathway is not derived from "2 + 2" here. Clearly, the ORRs electro-catalyzed by the Fe-NCNT@NiFe-LDH and Fe-NCNT both undergo the direct 4-electron pathway coupled with a small part (0–6%) of the 2-electron pathway.

Notably, the electrocatalysts that only lead a direct 4-electron pathway ORR can completely eliminate H_2O_2 production, which is extremely favorable to elevate their longevity to avoid any Fenton or Fenton-like corrosion reactions on their structures. Nevertheless, the byproduct H_2O_2 is always inevitably generated in ORRs (in the discharging process of ZABs). As revealed in Fig. S18 and S19 (ESI†), H_2O_2 was accumulated along with the discharging time in the simulated Zn–air discharging battery. Then, H_2O_2 could be decomposed to $^{\bullet}OH$ and $^{\bullet}OOH$ radicals *via* Fenton or Fenton-like reactions,[17] and the highly reactive $^{\bullet}OH$ radicals pose huge threats to the activity and long-term stability of catalysts (especially for Fe-containing carbons). As revealed in Fig. S20 (ESI†), once H_2O_2 encounters with the Fe species, $^{\bullet}OH$ and $^{\bullet}OOH$ will be generated even in an alkaline environment. In addition, structure destruction caused by the radical has been widely verified in proton exchange membrane fuel cells (PEMFCs)[75] and pollutant degradation.[76] As revealed here in Fig. S21 (ESI†), the molecular structure of RhB could be degraded in the alkaline solution with H_2O_2 and traces of Fe species. Analogously, if the radicals are generated *via* Fenton or Fenton-like reactions, they will pose huge threats to the ZABs. However, there are no reports on the effects and mechanisms of radicals on ZABs at present.

Based on the above-mentioned considerations, the exploration of the consumption pathways of H_2O_2 should be highly valued. In electrochemical batteries, H_2O_2 can be consumed *via* electrochemical and non-electrochemical pathways without forming $^{\bullet}OH$. In addition, there are two types of electrochemical pathways to consume H_2O_2, including peroxide reduction and oxidation reactions (PRR: H_2O_2 to OH^-; POR: H_2O_2 to oxygen; the detail reaction formulas are shown in ESI†).[77] The PRR and POR performances of the as-prepared catalysts were evaluated. In comparison with the NiFe-LDH, the Fe-NCNT@NiFe-LDH and Fe-NCNT both display high PRR and POR activities, suggesting that H_2O_2 could be electrochemically consumed conveniently (Fig. 5(e)). When comparing Fig. S22 with Fig. S18 (ESI†), it is revealed that almost two-thirds of H_2O_2 generated in the ORR process could be consumed *via* the POR (accompanied by the OER in the charging process of ZABs). In addition, the disproportionation reaction is another favorable way (also without forming $^{\bullet}OH$) to decompose H_2O_2. The Fe-NCNT@NiFe-LDH and Fe-NCNT both exhibit obvious catalytic ability to induce disproportionation of H_2O_2 to produce O_2 (measured by gas chromatography; more details are provided in Fig. S23 and Movies S3–S6, ESI†). As shown in Fig. 5(f), the oxygen production rate of the Fe-NCNT@NiFe-LDH is about twice that of the Fe-NCNT (in the first 25 min). After about half an hour, the Fe-NCNT@NiFe-LDH could produce 65.2 μmol of oxygen with a conversion of 22.5%, higher than those of the Fe-NCNT (47.5 μmol and 16.4%). The gas chromatography (GC) results indicate that the disproportionation effect of the Fe-NCNT is much enhanced by the NiFe-LDH *via* construction of wrapping structures, probably also resulting from the promotion of hydrophilicity, which thus facilitates the transportation of H_2O_2 to the catalyst surface. Finally, to probe whether H_2O_2 is decomposed *via* Fenton and Fenton-like reactions, the fluorescence method is introduced here, wherein terephthalic acid (PTA) is used to capture $^{\bullet}OH$ radicals to form 2-hydroxy terephthalic acid (a fluorescent material with a strong emission at ~425 nm).[78] Commonly, at around room temperature (30 °C is applied here), $^{\bullet}OH$ radicals cannot be formed from water without H_2O_2. As revealed in Fig. 5(g), there are no fluorescence peaks at around 425 nm. When 10 mM H_2O_2 was introduced (Fig. 5(h)), fluorescence peaks emerged. Notably, the fluorescence intensities are much weaker than those of the traditional Fenton reagent, *i.e.* Fe^{2+} ions + H_2O_2, suggesting that there are only a small number of $^{\bullet}OH$ radicals produced in these systems containing catalyst and H_2O_2 *via* Fenton or Fenton-like reactions (most Fe are embedded in nanotubes). Furthermore, to resemble the actual application, the as-prepared catalysts are undergoing ORRs continuously for 3 h (as revealed by RRDE, byproduct H_2O_2 is generated). As demonstrated in Fig. 5(i), there are a negligible number of $^{\bullet}OH$ radicals generated by these catalysts. Meanwhile, ESR was taken for the solution after ORR test (using Fe-NCNT@NiFe-LDH as the catalyst) for 3 h. It is revealed that the amounts of $^{\bullet}OH$ and $^{\bullet}OOH$ are below the detection limit. Notably, the fluorescent intensity shown in Fig. 5(h) and (i) follows the trend NiFe-LDH > Fe-NCNT > Fe-NCNT@NiFe-LDH, which is in accordance with the PRR/POR electrochemical test results and GC measurements. Taken together, due to excellent chemical and electrochemical catalytic abilities of the Fe-NCNT@NiFe-LDH (Fe-NCNT is next.) on H_2O_2, a considerable part of H_2O_2 is depleted *via* disproportionation and reduced electrochemically, thereby the amount of H_2O_2 involved in Fenton or Fenton-like reactions is substantially cut down.

Zn–air batteries (ZABs) were assembled using zinc plates as anodes and Pt/C + IrO_2, Fe-NCNT@NiFe-LDH, and Fe-NCNT respectively as air cathodes. The ZAB construction and working principle are schematically shown in Fig. 6(a). The ZAB based on the Fe-NCNT@NiFe-LDH, Fe-NCNT, and Pt/C + IrO_2 exhibits open-circuit voltages of 1.42 V, 1.36 V, and 1.43 V, respectively (Fig. S24, ESI†). The charging–discharging polarization curves of these ZABs were measured to preliminarily evaluate their application potential. As revealed in Fig. S25 (ESI†), the Fe-NCNT@NiFe-LDH-based device possesses a smaller voltage gap

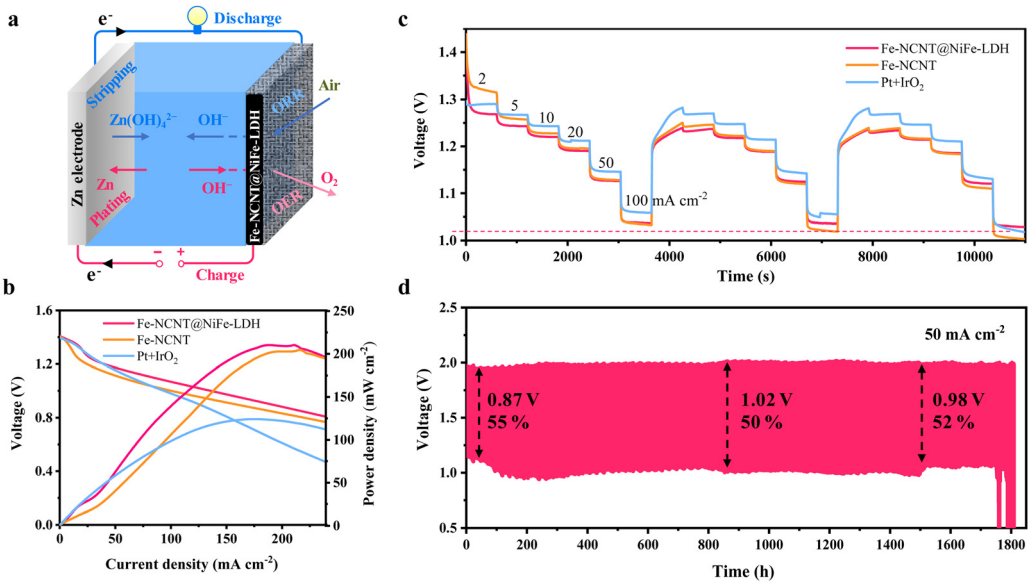

Fig. 6 (a) Schematic structure of liquid rechargeable ZABs. (b) Discharging polarization and corresponding power density curves of Fe-NCNT@NiFe-LDH-based, Fe-NCNT-based and Pt/C + IrO_2-based ZABs. (c) Discharging voltages at current densities of 2, 5, 10, 20, 50 and 100 mA cm^{-2} for these ZABs, respectively. (d) Long charging and discharging cycle performance of Fe-NCNT@NiFe-LDH-based ZABs at a current density of 50 mA cm^{-2}.

in the whole applied voltage. Corresponding to 50 and 100 mA cm^{-2}, the voltage gaps are 0.62 and 0.93 V for the Fe-NCNT@NiFe-LDH, 0.73 and 1.04 V for the Fe-NCNT, and 0.74 and 1.10 V for Pt/C + IrO_2-based devices. Fig. 6(b) displays the discharging polarization and calculated power-density curves of these ZABs. The maximum output power density of the Fe-NCNT@NiFe-LDH-based ZAB is 204 mW cm^{-2}, outperforming Fe-NCNT ZABs (200 mW cm^{-2}) and Pt/C + IrO_2 ZABs (124 mW cm^{-2}). Fig. 6(c) displays the discharging rate performances of these ZABs. In comparison with Pt/C + IrO_2 and Fe-NCNT, Fe-NCNT@NiFe-LDH-assembled ZABs can well maintain the discharging voltage even cycling at a high current density ranging from 2 to 100 mA cm^{-2} for three times. Specifically, in the three cycles, the Fe-NCNT@NiFe-LDH-assembled ZAB exhibits stable voltage platforms of 1.23, 1.22, 1.19, 1.12, and 1.03 V at 5, 10, 20, 50 and 100 mA cm^{-2}. The discharging rate performance test clearly suggests that the Fe-NCNT@NiFe-LDH possesses extraordinary rate performance. Furthermore, long-term discharging/charging cycling tests were carried out. As represented in Fig. 6(d), the battery with the Fe-NCNT@NiFe-LDH cathode exhibits an extremely long lifespan of 1743 h (5229 cycles), an average voltage gap of only 0.96 V, and a high average round-trip efficiency of 52.3% at 50 mA cm^{-2}. Specifically, the cell demonstrates an initial round-trip efficiency of 56% with a discharging voltage of 1.95 V and a charging voltage of 1.08 V. After 870 h (2610 cycles) of continuous discharging/charging cycling, the round-trip efficiency decreases to 50%. After 1530 h (4590 cycles), the round-trip efficiency increases slightly to 52%, probably because upon entering into spring, the room temperature is raised. When the current density is raised up to 100 mA cm^{-2} (Fig. S26, ESI†), the Fe-NCNT@NiFe-LDH ZAB could withstand the continuous discharging/charging cycles for nearly 80 hours with an average voltage gap of 1.39 V. For comparing, the charging/discharging cycling performances of Fe-NCNT@NiFe-LDH and Fe-NCNT ZABs were measured at 10 mA cm^{-2}. As revealed in Fig. S27 (ESI†), the Fe-NCNT@NiFe-LDH preserves a long lifespan of 1777 h and maintains an average voltage gap of 0.73 V and an energy efficiency of 0.62; in contrast, Fe-NCNT ZABs (Fig. S28, ESI†) exhibit an enlarged average voltage gap of 0.95 V with an energy efficiency of 0.51 and an obviously short working period of about 800 h. The remarkable durability and low charging–discharging voltage gap of Fe-NCNT@NiFe-LDH-based ZABs are attributed to the unique NiFe-LDH encapsulation structure with extremely improved electrocatalytic OER and ORR bifunction and enhanced material stability.

Conclusion

In summary, a composite has been constructed with the structure of NiFe-LDH nanosheets tightly and uniformly wrapped on N-doped carbon nanotubes embedded with Fe NPs. The NiFe-LDH wrapper significantly enhances the OER electrocatalytic activity of the Fe-NCNT@NiFe-LDH composite and simultaneously promotes its ORR performance especially at large current density. As a result, the Fe-NCNT@NiFe-LDH exhibits an exceedingly small ΔE of 0.52 V. Furthermore, the electrochemical oxidation and corrosion of Fe-NCNTs can be alleviated to a large extent during the charging process of Zn–air batteries (ZABs), because of protection by OER highly active NiFe-LDH nanosheets *via* preferentially taking the OER catalyzing role and, meanwhile, decreasing the charging potential. Additionally, it was found that the Fe-NCNT@NiFe-LDH is highly effective in consuming peroxides *via* disproportionation and electrochemical oxidation and reduction (PRR and POR) reactions. These consuming processes unavoidably depress the radical-formation

paths, which protects the catalyst from radical (such as •OH) attacks and, thus, enormously enhance the catalyst durability. The Fe-NCNT@NiFe-LDH-based conventional two-electrode ZAB achieved an extremely high lifespan of 1777 hours and a low voltage gap of 0.73 V at a current density of 10 mA cm^{-2}, and a lifespan of 1743 hours and a voltage gap of 0.96 V at a current density of 50 mA cm^{-2}.

Author contributions

Jiale Li: investigation, interpretation of the data, validation, and writing. Minghui Lv, Na Su, Chao Li, and Yongye Wang: investigation and formal analysis. Yingping Huang, Yong Zheng, and Wei Liu: formal analysis and conceptualization. Niu Huang, Tianyi Ma, and Liqun Ye: conceptualization, methodology, supervision, funding acquisition, and writing.

Conflicts of interest

The authors declare no competing interests.

Acknowledgements

This work is supported by the National Natural Science Foundation of China (no. 51872147, 22136003), Project of Hubei Provincial Department of Education (D20221202), and the 111 Project (D20015).

References

1 M. Luo, Z. Zhao, Y. Zhang, Y. Sun, Y. Xing, F. Lv, Y. Yang, X. Zhang, S. Hwang, Y. Qin, J. Y. Ma, F. Lin, D. Su, G. Lu and S. Guo, *Nature*, 2019, **574**, 81–85.
2 Q. Wang, Q. Feng, Y. Lei, S. Tang, L. Xu, Y. Xiong, G. Fang, Y. Wang, P. Yang, J. Liu, W. Liu and X. Xiong, *Nat. Commun.*, 2022, **13**, 3689.
3 F. Shi, K. Zhu, X. Li, E. Wang, X. Zhu and W. Yang, *J. Energy Chem.*, 2021, **61**, 327–335.
4 D. Lyu, S. Yao, A. Ali, Z. Q. Tian, P. Tsiakaras and P. K. Shen, *Adv. Energy Mater.*, 2021, **11**, 2101249.
5 M. Goswami, S. Mandal and V. K. Pillai, *Sci. Rep.*, 2023, **13**, 5182.
6 J. T. Mefford, A. R. Akbashev, M. Kang, C. L. Bentley, W. E. Gent, H. D. Deng, D. H. Alsem, Y. S. Yu, N. J. Salmon, D. A. Shapiro, P. R. Unwin and W. C. Chueh, *Nature*, 2021, **593**, 67–73.
7 M. Lv, C. Luo, J. Li, Y. Zhang, Q. Zeng, N. Huang, S. Wang, Y. Zheng, W. Liu and L. Ye, *ACS Mater. Lett.*, 2023, **5**, 744–752.
8 Y. Meng, Y. M. Zhao, J. C. Li, C. Shi, L. Zhang, P. X. Hou, C. Liu and H. M. Cheng, *NPG Asia Mater.*, 2023, **15**, 14.
9 X. Zhong, Y. Shao, B. Chen, C. Li, J. Sheng, X. Xiao, B. Xu, J. Li, H. M. Cheng and G. Zhou, *Adv. Mater.*, 2023, 2301952.
10 G. Li, Y. Tang, T. Fu, Y. Xiang, Z. Xiong, Y. Si, C. Guo and Z. Jiang, *Chem. Eng. J.*, 2022, **429**, 132174.
11 K. Sheng, Q. Yi, A. L. Chen, Y. Wang, Y. Yan, H. Nie and X. Zhou, *ACS Appl. Mater. Interfaces*, 2021, **13**, 45394–45405.
12 L. Yang, N. Huang, C. Luo, H. Yu, P. Sun, X. Lv and X. Sun, *Chem. Eng. J.*, 2021, **404**, 127112.
13 Q. Wang, Y. Yang, F. Sun, G. Chen, J. Wang, L. Peng, W. T. Chen, L. Shang, J. Zhao, D. Sun Waterhouse, T. Zhang and G. I. N. Waterhouse, *Adv. Energy Mater.*, 2021, **11**, 2100219.
14 X. Wan, Q. Liu, J. Liu, S. Liu, X. Liu, L. Zheng, J. Shang, R. Yu and J. Shui, *Nat. Commun.*, 2022, **13**, 2963.
15 Q. Ma, H. Jin, J. Zhu, Z. Li, H. Xu, B. Liu, Z. Zhang, J. Ma and S. Mu, *Adv. Sci.*, 2021, **8**, 2102209.
16 H. Li, N. Cheng, Y. Zheng, X. Zhang, H. Lv, D. He, M. Pan, F. Kleitz, S. Z. Qiao and S. Mu, *Adv. Energy Mater.*, 2013, **3**, 1176–1179.
17 Z. Deng, M. Gong, Z. Gong and X. Wang, *Nano Lett.*, 2022, **22**, 9551–9558.
18 Y. Shao, J. P. Dodelet, G. Wu and P. Zelenay, *Adv. Mater.*, 2019, **31**, 1807615.
19 H. Xie, X. Xie, G. Hu, V. Prabhakaran, S. Saha, L. Gonzalez-Lopez, A. H. Phakatkar, M. Hong, M. Wu, R. Shahbazian-Yassar, V. Ramani, M. I. Al-Sheikhly, D. Jiang, Y. Shao and L. Hu, *Nat. Energy*, 2022, **7**, 281–289.
20 Y. T. Liu, L. Tang, J. Dai, J. Yu and B. Ding, *Angew. Chem., Int. Ed.*, 2020, **59**, 13623–13627.
21 S. Cao, H. Huang, K. Shi, L. Wei, N. You, X. Fan, Z. Yang and W. Zhang, *Chem. Eng. J.*, 2021, **422**, 130123.
22 H. Lei, Z. Wang, F. Yang, X. Huang, J. Liu, Y. Liang, J. Xie, M. S. Javed, X. Lu, S. Tan and W. Mai, *Nano Energy*, 2020, **68**, 104293.
23 F. Zhou, X. Zhang, R. Sa, S. Zhang, Z. Wen and R. Wang, *Chem. Eng. J.*, 2020, **397**, 125454.
24 K. Obata and K. Takanabe, *Angew. Chem., Int. Ed.*, 2018, **57**, 1616–1620.
25 Q. Liang, H. Jin, Z. Wang, Y. Xiong, S. Yuan, X. Zeng, D. He and S. Mu, *Nano Energy*, 2019, **57**, 746–752.
26 S. Liu, S. Geng, L. Li, Y. Zhang, G. Ren, B. Huang, Z. Hu, J. F. Lee, Y. H. Lai, Y. H. Chu, Y. Xu, Q. Shao and X. Huang, *Nat. Commun.*, 2022, **13**, 1187.
27 P. Liu, B. Chen, C. Liang, W. Yao, Y. Cui, S. Hu, P. Zou, H. Zhang, H. J. Fan and C. Yang, *Adv. Mater.*, 2021, **33**, 2007377.
28 W. Huang, J. Li, X. Liao, R. Lu, C. Ling, X. Liu, J. Meng, L. Qu, M. Lin, X. Hong, X. Zhou, S. Liu, Y. Zhao, L. Zhou and L. Mai, *Adv. Mater.*, 2022, **34**, 2200270.
29 W. H. Lee, M. H. Han, Y. J. Ko, B. K. Min, K. H. Chae and H. S. Oh, *Nat. Commun.*, 2022, **13**, 605.
30 W. Cheng, S. Xi, Z. P. Wu, D. Luan and X. W. Lou, *Sci. Adv.*, 2021, **7**, eabk0919.
31 Y. Wang, X. Li, M. Zhang, J. Zhang, Z. Chen, X. Zheng, Z. Tian, N. Zhao, X. Han, K. Zaghib, Y. Wang, Y. Deng and W. Hu, *Adv. Mater.*, 2022, **34**, 2107053.
32 J. Kwon, H. Han, S. Jo, S. Choi, K. Y. Chung, G. Ali, K. Park, U. Paik and T. Song, *Adv. Energy Mater.*, 2021, **11**, 2100624.
33 Z. Liang, N. Kong, C. Yang, W. Zhang, H. Zheng, H. Lin and R. Cao, *Angew. Chem., Int. Ed.*, 2021, **60**, 12759–12764.

34 C. Wang, P. Zhai, M. Xia, Y. Wu, B. Zhang, Z. Li, L. Ran, J. Gao, X. Zhang, Z. Fan, L. Sun and J. Hou, *Angew. Chem., Int. Ed.*, 2021, **60**, 27126–27134.
35 X. Qiao, H. Kang, Y. Li, K. Cui, X. Jia, X. Wu and W. Qin, *Small*, 2022, **18**, 2106378.
36 T. Wang, P. Wang, W. Zang, X. Li, D. Chen, Z. Kou, S. Mu and J. Wang, *Adv. Funct. Mater.*, 2021, **32**, 2107382.
37 C. X. Zhao, J. N. Liu, J. Wang, D. Ren, J. Yu, X. Chen, B. Q. Li and Q. Zhang, *Adv. Mater.*, 2021, **33**, 2008606.
38 Y. Han, H. Duan, C. Zhou, H. Meng, Q. Jiang, B. Wang, W. Yan and R. Zhang, *Nano Lett.*, 2022, **22**, 2497–2505.
39 T. Wang, Y. Han, P. Xu, X. Feng, W. Ji and H. Arandiyan, *Chem. Eng. J.*, 2022, **450**, 138245.
40 D. Chen, X. Chen, Z. Cui, G. Li, B. Han, Q. Zhang, J. Sui, H. Dong, J. Yu and L. Yu, *Chem. Eng. J.*, 2020, **399**, 125718.
41 S. Y. Lin, X. Zhang, S. Y. Sang, L. Zhang, J. J. Feng and A. Wang, *J. Colloid Interface Sci.*, 2022, **628**, 499.
42 C. Zhou, X. Chen, S. Liu, Y. Han, H. Meng, Q. Jiang, S. Zhao, F. Wei, J. Sun, T. Tan and R. Zhang, *J. Am. Chem. Soc.*, 2022, **144**, 2694–2704.
43 M. Zhang, J. Zhang, S. Ran, L. Qiu, W. Sun, Y. Yu, J. Chen and Z. Zhu, *Nano Res.*, 2020, **14**, 1175–1186.
44 X. Li, Y. Liu, H. Chen, M. Yang, D. Yang, H. Li and Z. Lin, *Nano Lett.*, 2021, **21**, 3098–3105.
45 X. Chen, D. Chen, G. Li, P. Sha, J. Yu, L. Yu and L. Dong, *Electrochim. Acta*, 2022, **428**, 140938.
46 Y. Wang, G. Zhang, M. Ma, Y. Ma, J. Huang, C. Chen, Y. Zhang, X. Sun and Z. Yan, *Sci. China Mater.*, 2020, **63**, 1182–1195.
47 Y. Tang, Y. Lei, G. Li, T. Fu, Y. Xiang, J. Sha, H. Yang, P. Yu, Y. Si and C. Guo, *J. Mater. Chem. A*, 2022, **10**, 5305–5316.
48 O. Ambriz-Peláez, J. Béjar, C. M. Ramos-Castillo, M. Guerra-Balcázar, L. Álvarez-Contreras and N. Arjona, *Appl. Surf. Sci.*, 2022, **601**, 1154253.
49 X. Feng, Q. Jiao, W. Chen, Y. Dang, Z. Dai, S. L. Suib, J. Zhang, Y. Zhao, H. Li and C. Feng, *Appl. Catal., B*, 2021, **286**, 119869.
50 T. Hu, Z. Jiang, Z. Fu and Z. Jiang, *J. Mater. Chem. A*, 2022, **10**, 8739–8750.
51 Y. Niu, X. Teng, S. Gong and Z. Chen, *J. Mater. Chem. A*, 2020, **8**, 13725–13734.
52 C. Lai, M. Gong, Y. Zhou, J. Fang, L. Huang, Z. Deng, X. Liu, T. Zhao, R. Lin, K. Wang, K. Jiang, H. Xin and D. Wang, *Appl. Catal., B*, 2020, **274**, 119086.
53 Y. Xiang, C. Xu, T. Fu, Y. Tang, G. Li, Z. Xiong, C. Guo and Y. Si, *Appl. Surf. Sci.*, 2022, **575**, 151730.
54 X. Chen, J. Pu, X. Hu, Y. Yao, Y. Dou, J. Jiang and W. Zhang, *Small*, 2022, **18**, 2200578.
55 K. Khan, X. Yan, Q. Yu, S. H. Bae, J. J. White, J. Liu, T. Liu, C. Sun, J. Kim and H. M. Cheng, *Nano Energy*, 2021, **90**, 106488.
56 M. Jiang, Z. Tan and M. Cao, *Int. J. Hydrogen Energy*, 2021, **46**, 15507–15516.
57 D. Wu, X. Hu, Z. Yang, T. Yang, J. Wen, G. Lu, Q. Zhao, Z. Li, X. Jiang and C. Xu, *Ind. Eng. Chem. Res.*, 2022, **61**, 7523–7528.
58 Y. Hao, Y. Kang, H. Kang, H. Xin, F. Liu, L. Li, W. Wang and Z. Lei, *J. Power Sources*, 2022, **524**, 231076.
59 W. Li, Y. Wu, M. Chen, P. Dai, T. Jiang and S. Zhou, *J. Alloys Compd.*, 2022, **925**, 166658.
60 Y. Ma, W. Chen, Z. Jiang, X. Tian, X. WangGuo, G. Chen and Z.-J. Jiang, *J. Mater. Chem. A*, 2022, **10**, 12616–12631.
61 L. Lin, P. Xue, X. Cui, J. Liu, J. Liu, M. Tang and Z. Wang, *J. Alloys Compd.*, 2022, **909**, 164625.
62 R. M. Sun, L. Zhang, J. J. Feng, K. M. Fang and A. J. Wang, *J. Colloid Interface Sci.*, 2022, **608**, 2100–2110.
63 L. Wu, R. Zhao, G. Du, H. Wang, M. Hou, W. Zhang, P. Sun and T. Chen, *Green Energy Environ.*, 2022, DOI: **10.1016/j.gee.2022.03.014**.
64 J. Yu, Y. Dai, Z. Zhang, T. Liu, S. Zhao, C. Cheng, P. Tan, Z. Shao and M. Ni, *Carbon Energy*, 2022, **4**, 576–585.
65 Y. Liu, Z. Chen, N. Zhao, G. Tong, Z. Li, B. Wang, Y. Du, Q. Pan, Z. Li and Y. Xie, *Chem. Eng. J.*, 2022, **433**, 134469.
66 R. Hao, J. Chen, Z. Wang, Y. Huang, P. Liu, J. Yan, K. Liu, C. Liu and Z. Lu, *J. Colloid Interface Sci.*, 2021, **586**, 621–629.
67 Y. Kang, W. Wang, J. Li, S. Imhanria, Y. Hao and Z. Lei, *J. Power Sources*, 2021, **493**, 229665.
68 P. Liu, G. Cheng, G. Liu, M. Sun, S. Fu, Z. Zhou, S. Han and L. Yu, *J. Mater. Sci.: Mater. Electron.*, 2021, **32**, 14385–14397.
69 Y. Zhang, X. P. Kong, X. Lin, K. Hu, W. Zhao, G. Xie, X. Lin, X. Liu, Y. Ito and H. J. Qiu, *J. Energy Chem.*, 2022, **66**, 466–473.
70 Y. Zhang, W. Shi, L. Bo, Y. Shen, X. Ji, L. Xia, X. Guan, Y. Wang and J. Tong, *Chem. Eng. J.*, 2022, **431**, 134188.
71 Y. Ren, H. Wang, T. Zhang, L. Ma, P. Ye, Y. Zhong and Y. Hu, *Chin. Chem. Lett.*, 2021, **32**, 2243–2248.
72 X. Hui, P. Zhang, Z. Wang, D. Zhao, Z. Li, Z. Zhang, C. Wang and L. Yin, *ACS Appl. Energy Mater.*, 2022, **5**, 6100–6109.
73 J. Liu, Z. Gong, C. Allen, W. Ge, H. Gong, J. Liao, J. Liu, K. Huang, M. Yan, R. Liu, G. He, J. Dong, G. Ye and H. Fei, *Chem. Catal.*, 2021, **1**, 1291–1307.
74 G. I. Berglund, G. H. Carlsson, A. T. Smith, H. Szöke, A. Henriksen and J. Hajdu, *Nature*, 2002, **417**, 463–468.
75 K. Kodama, T. Nagai, A. Kuwaki, R. Jinnouchi and Y. Morimoto, *Nat. Nanotechnol.*, 2021, **16**, 140–147.
76 X. Yang, Y. Ye, J. Sun, Z. Li, J. Ping and X. Sun, *Small*, 2022, **18**, 2105089.
77 Q. Zhang, P. Kumar, X. Zhu, R. Daiyan, N. M. Bedford, K. H. Wu, Z. Han, T. Zhang, R. Amal and X. Lu, *Adv. Energy Mater.*, 2021, **11**, 2100303.
78 B. Yan, Z. Shi, J. Lin, L. Zhang, L. Han, X. Shi and Q. Yang, *Environ. Sci.: Nano*, 2022, **9**, 532–541.